Temperature and Wind Climate of the Antarctic Peninsula as Simulated by a High-Resolution Regional Atmospheric Climate Model

JAN MELCHIOR VAN WESSEM, CARLEEN H. REIJMER, WILLEM JAN VAN DE BERG, AND MICHIEL R. VAN DEN BROEKE

Institute for Marine and Atmospheric Research Utrecht, Utrecht University, Utrecht, Netherlands

ALISON J. COOK

Department of Geography, Swansea University, Swansea, United Kingdom

LAMBERTUS H. VAN ULFT AND ERIK VAN MEIJGAARD

Royal Netherlands Meteorological Institute, De Bilt, Netherlands

(Manuscript received 20 January 2015, in final form 15 June 2015)

ABSTRACT

The latest polar version of the Regional Atmospheric Climate Model (RACMO2.3) has been applied to the Antarctic Peninsula (AP). In this study, the authors present results of a climate run at 5.5 km for the period 1979–2013, in which RACMO2.3 is forced by ERA-Interim atmospheric and ocean surface fields, using an updated AP surface topography. The model results are evaluated with near-surface temperature and wind measurements from 12 manned and automatic weather stations and vertical profiles from balloon soundings made at three stations. The seasonal cycle of near-surface temperature and wind is simulated well, with most biases still related to the limited model resolution. High-resolution climate maps of temperature and wind showing that the AP climate exhibits large spatial variability are discussed. Over the steep and high mountains of the northern AP, large west-to-east climate gradients exist, while over the gentle southern AP mountains the near-surface climate is dominated by katabatic winds. Over the flat ice shelves, where katabatic wind forcing is weak, interannual variability in temperature is largest. Finally, decadal trends of temperature and wind are presented, and it is shown that recently there has been distinct warming over the northwestern AP and cooling over the rest of the AP, related to changes in sea ice cover.

1. Introduction

Over the past 50 years, the Antarctic Peninsula (AP) has experienced warming that is significantly greater than the rest of the Antarctic continent and possibly greater than all other regions on Earth (Turner et al. 2005). This resulted in the (partial) disintegration of multiple ice shelves that fringe the AP [e.g., Larsen A, Larsen B, and parts of the Wilkins Ice Shelf (Cook and Vaughan 2010)]. In turn, this led to the speedup and thinning of the grounded glaciers that feed into these ice shelves (Scambos 2004; Rott et al. 2011) and consequently to an increased grounded ice discharge and contribution of AP glaciers to global sea level rise (Rignot et al. 2004). Although the exact cause of AP ice shelf disintegration is still under debate, it is generally believed that the disintegration of Larsen A and B ice shelves was mainly driven by enhanced surface melt in response to stronger atmospheric westerlies in summer (van Lipzig et al. 2008; Marshall et al. 2006), resulting in meltwater ponding and hydrofracturing (Scambos et al. 2000; Van den Broeke et al. 2005; Scambos et al. 2009).

The climate of the AP is shaped by its narrow mountain range, which acts as a barrier to the Southern Hemisphere westerlies, introducing large horizontal gradients in temperature and precipitation. Moreover, AP temperatures are sensitive to sea ice cover in the Bellingshausen Sea, especially in winter (King 1994). To understand recent changes, continuous records of temperature, wind, and pressure are available from manned surface and automatic weather stations mainly along the western and northern AP

Corresponding author address: Jan Melchior van Wessem, Princetonplein 5, Utrecht 3584 CC, the Netherlands.
E-mail: j.m.vanwessem@uu.nl

DOI: 10.1175/JCLI-D-15-0060.1

coast. Some of these time series date back to well before the International Geophysical Year of 1957–58. The automatic weather stations and the manned stations combined now provide a reasonable spatial coverage of the AP (Turner et al. 2005). Nevertheless, large regions of the AP remain devoid of data because of the steep mountain slopes and the harsh climatic conditions, including extreme amounts of precipitation, especially on the western side (Genthon and Krinner 2001). To fill these gaps, remote sensing techniques can be used, such as microwave sensors to detect (brightness) temperatures (Tedesco et al. 2007) or radar backscatter to identify melt episodes (Barrand et al. 2013). Atmospheric reanalysis products (Bracegirdle and Marshall 2012) and global climate models (GCMs) provide gridded climate information, but with horizontal resolutions that range from 25 to 150 km, these do not accurately resolve the rough topography of the AP. Dynamical downscaling using high-resolution regional atmospheric climate models (RCMs) has proven to be a good method to represent climate at 5–10-km resolution. Moreover, RCMs can be specifically adapted to simulate the climate and surface mass balance of glaciated regions, such as the Antarctic ice sheet (Lenaerts et al. 2012c; Van Wessem et al. 2014b), but also of smaller partly glaciated regions, such as Greenland (Fettweis 2007; Ettema et al. 2010), Patagonia (Lenaerts et al. 2014), and Svalbard (Claremar et al. 2012; Lang et al. 2015).

Previous simulations of AP climate only covered short time spans because of limited computational resources (Van Lipzig et al. 2004), lacked the resolution to accurately resolve the topography of the AP (Van Wessem et al. 2014b), or were performed for operational purposes by short-range forecast models (Powers et al. 2012) with changing physics. Here, we use the Regional Atmospheric Climate Model, version 2.3 (RACMO2.3), to simulate the AP climate at a relatively high horizontal resolution of ~5.5 km and the longest period for which reliable forcing is available (1979–2013). We evaluate the simulated near-surface temperature and wind fields over the AP by comparing model output with observations from 12 manned and automatic weather stations and using profile data from balloon soundings. Section 2 presents the RACMO2.3 model and the observational data used; section 3 discusses the model evaluation; and section 4 presents high-resolution maps of modeled temperature and wind, followed by conclusions in section 5.

2. Data and methods

a. Regional Atmospheric Climate Model

The Regional Atmospheric Climate Model, version 2.3, combines the dynamics package of the High Resolution Limited Area Model (HIRLAM; Undén et al. 2002) with the physics package of the European Centre for Medium-Range Weather Forecasts (ECMWF) Integrated Forecast System (IFS). RACMO2.3 has been adapted for use over the large ice sheets of Greenland and Antarctica (Reijmer et al. 2005); it includes a multilayer snow model to calculate melt, percolation, refreezing, and runoff of liquid water (Ettema et al. 2010); a prognostic scheme for snow grain size to calculate surface albedo (Kuipers Munneke et al. 2011); and a routine that simulates the interaction of drifting snow with the surface and the lower atmosphere (Lenaerts et al. 2012a). ERA-Interim data with 6-hourly resolution from January 1979 to December 2013 (Dee et al. 2011) are used to force the model at the lateral atmospheric boundaries as well as at the lower ocean boundaries by prescribing sea ice fraction and sea surface temperatures. Tests with different relaxation zones have confirmed that the relaxation zone is sufficiently wide that the model interior (Fig. 1) is allowed to evolve independently of the lateral boundary relaxation. A model time step of 2 min is used.

RACMO2.3 is a hydrostatic model that we run at a horizontal resolution of ~5.5 km and 40 vertical levels. The high horizontal model resolution is a significant improvement over previous RACMO simulations of Antarctica, which used horizontal resolutions of 55, 27, and 14 km respectively. We assume hydrostatic balance to hold at 5.5-km horizontal resolution: the validity of this assumption is confirmed by the fact that RACMO2.3 output agrees very well with surface and upper-air observations (see section 3), although obviously there would be processes that will be better resolved in a nonhydrostatic model [e.g., winds over sloping surfaces (Cassano and Parish 2000)]. The surface topography is based on the 100-m digital elevation model (DEM) from Cook et al. (2012) for the grounded ice sheet north of 70°S and on the 1-km DEM from Bamber and Gomez-Dans (2009) for the ice shelves and the remainder of the domain. This is a major update of the previous model topography, which was based on the Radarsat Antarctic Mapping Project, version 2, DEM (RAMPv2 DEM; Liu et al. 2001). The ice sheet mask is kept constant through the simulation and includes the (former) Larsen B and Larsen A ice shelves. For further details on the model, the reader is referred to Van Wessem et al. (2014a,b).

The model is initialized on 1 January 1979, with the atmospheric state and sea surface boundary conditions adopted from ERA-Interim. The initial firn pack of the AP is inferred from a simulation with an offline firn densification model (FDM; Ligtenberg et al. 2011), which was driven by an earlier simulation of the AP climate by RACMO2.3, largely comparable to the one

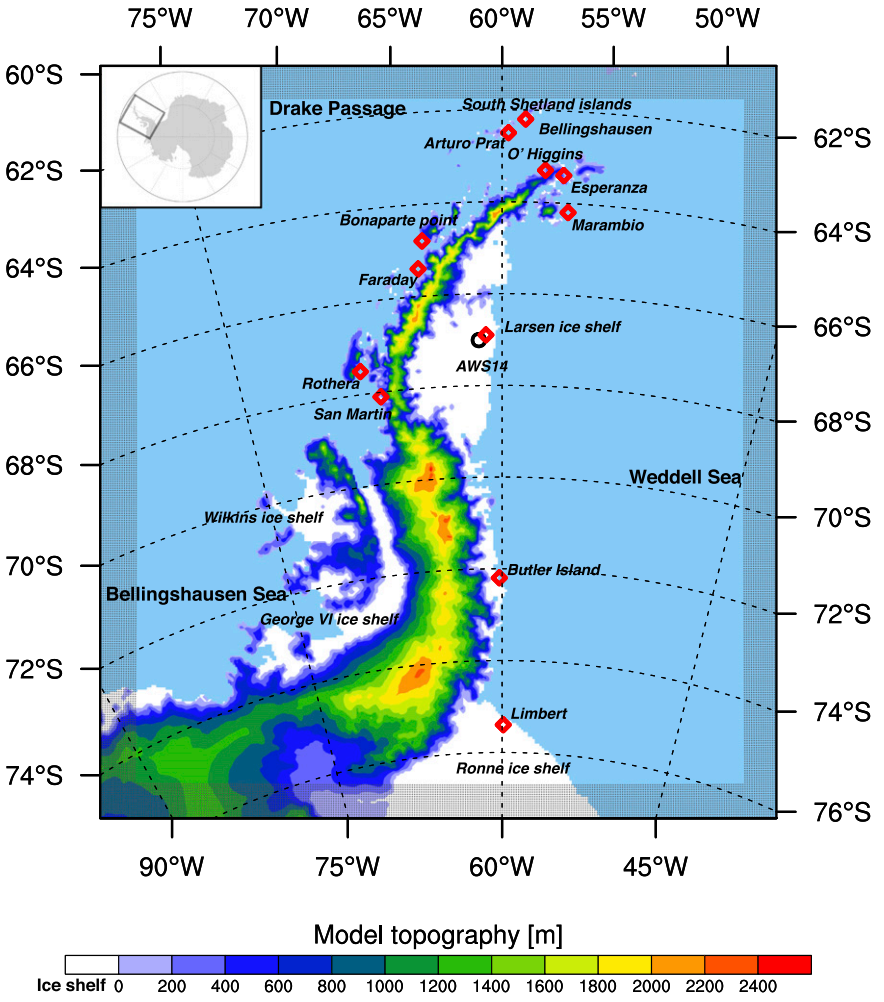

FIG. 1. RACMO2.3 Antarctic Peninsula model domain (black box in inset map of Antarctica), boundary relaxation zone (dotted area, 16 grid points) and surface topography (m) of the Antarctic Peninsula. Locations of SCAR-READER surface stations are marked (red diamonds), as is the location of AWS 14 (black circle). Model topography is based on digital elevation models from Cook et al. (2012) and Bamber and Gomez-Dans (2009). White areas represent the floating ice shelves; colors represent the elevation of the grounded ice sheet.

used in this study. More details on the FDM can be found in Ligtenberg et al. (2011).

b. *Observational data*

1) SCAR-READER STATIONS

To evaluate RACMO2.3 we use temperature and wind observations from the Scientific Committee on Antarctic Research (SCAR) Reference Antarctic Data for Environmental Research (READER; Turner et al. 2004) manned stations and automatic weather stations (AWS). The locations of these stations are marked in Fig. 1, and details are given in Table 1. We have omitted stations with time series <10 yr and stations that are located within a distance of $\sim$10 km (2 grid boxes) from other stations, choosing the one with the longer time series. For the remaining 12 SCAR-READER stations, we extracted monthly averaged values of air temperature and wind speed/direction from 1979 onward. As there are considerable elevation differences between model topography and the actual topography for the western AP stations, modeled temperature is corrected using a constant lapse rate of 7.2 K km^{-1} (Morris and Vaughan 2003). Output is not corrected for sensor height differences or variations (see Table 1). More information about the SCAR-READER stations and their data quality is given in Turner et al. (2004).

TABLE 1. Topographic and climatological information for the 12 SCAR-READER stations used in this study. For air temperature $T_{2\,m}$ and wind speed $V_{10\,m}$, starting years and number of available/total months are given. All time series run until December 2013. Between parentheses, M denotes a manned surface station, A denotes an automatic weather station, and UA denotes a manned station with upper-air measurements (2002–13). Sensor heights for $T_{2\,m}$ are 2 m for manned stations and variable (~3 m) for automatic weather stations. Sensor heights for $V_{10\,m}$ are 10 m for manned stations and variable (~5 m) for automatic weather stations. Data are not corrected for differences between sensor and model height.

Name	Lat (°S)	Lon (°W)	Elevation (m)	Start $T_{2\,m}$	Months $T_{2\,m}$	Start $V_{10\,m}$	Months $V_{10\,m}$
Arturo Prat (M)	62.5	59.7	5	1979	326/420	1983	260/372
Bellingshausen (M, UA)	62.2	58.9	16	1979	420/420	1979	420/420
Bonaparte Point (A)	64.8	64.1	8	1992	161/264	1992	121/264
Butler Island (A)	72.2	60.2	91	1986	285/336	1986	196/336
Esperanza (M)	63.4	57.0	13	1979	407/420	1979	389/420
Faraday/Vernadsky (M)	65.4	64.4	11	1979	416/420	1979	413/420
Larsen Ice Shelf (A)	67.0	67.0	32	1985	228/348	1985	222/348
Limbert (A)	75.4	59.9	40	1995	164/228	1995	91/228
Marambio (M, UA)	64.2	56.79	189	1979	413/420	1995	91/228
O'Higgins (M)	63.3	57.9	10	1979	366/420	1983	259/372
Rothera (M, UA)	67.4	68.1	32	1979	418/420	1979	417/420
San Martin (M)	68.1	67.1	54	1979	269/420	1979	217/420

2) BALLOON SOUNDINGS

At the manned surface stations of Rothera, Bellingshausen, and Marambio (Fig. 1), regular (1200 UTC) balloon soundings are performed to measure vertical profiles of temperature, wind speed, and wind direction. We use the upper-air monthly climatology (2002–13) of these stations from the SCAR-READER database to assess the quality of simulated RACMO2.3 upper-air conditions. In addition, at AWS 14 on the Larsen Ice Shelf (LIS), during a short experimental campaign in January 2011 and at irregular intervals, additional balloon soundings were performed (Kuipers Munneke et al. 2012). Two of these profiles are used together with simultaneous Rothera soundings to evaluate RACMO2.3-modeled gradients across the AP mountain range.

3. Results: Model evaluation

a. Near-surface temperature

Figure 2 shows modeled versus observed average (1979–2013), yearly, and monthly 2-m temperature at the 12 SCAR-READER stations. The stations include a broad range of annual mean temperatures, from the cold (~250 K) southeastern ice shelves toward the warm (~270 K) northern and western regions of the AP (see Table 2). Interannual variability (one standard deviation, expressed as error bars) is relatively low and similar for all stations. Figure 2 demonstrates that RACMO2.3 accurately simulates average near-surface (i.e., 2 m) temperature, both east and west of the mountain range. The coefficient of determination of all monthly values is high ($r^2 = 0.97$), partly because of the annual cycle being retained in the comparison, and overall temperature is slightly underestimated by the model (bias = −0.17 K), mostly because of an underestimation of summer temperatures. Individual station statistics are presented in Table 2: for all stations, the coefficient of determination is high ($r^2 > 0.9$), and biases are generally less than 1 K.

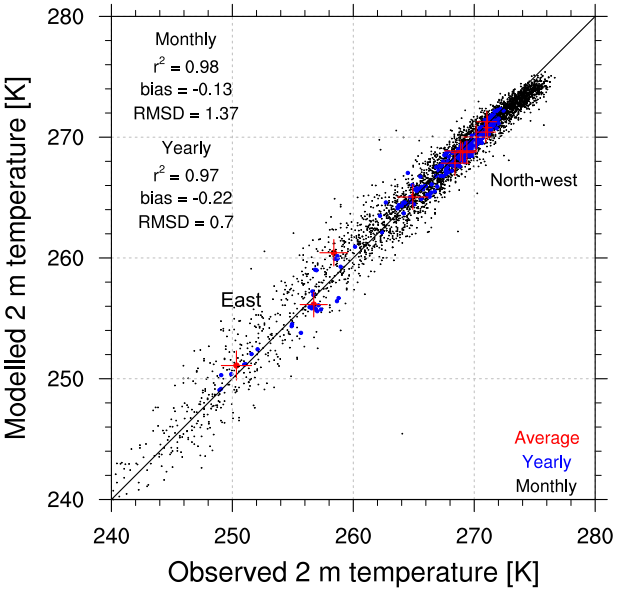

FIG. 2. Modeled vs 1979–2013 observed average (red), yearly (blue), and monthly (black) 2-m temperature $T_{2\,m}$(K). Red error bars denote interannual variability (1σ). For annual and yearly average values, the only years used are those that include observations for all 12 months. Coefficients of determination r^2, bias, and root-mean-square deviation (RMSD) of all monthly and yearly data are shown. The black line represents the 1:1 line.

TABLE 2. Observed (12 SCAR-READER stations) mean, bias (model − observation), standard deviation of the bias σ, root-mean-square deviation, and coefficient of determination r^2 (all with significance level $p < 0.0001$) of all individual (not detrended) monthly 2-m temperatures $T_{2\,m}$ (K). Modeled temperature is corrected for elevation differences between model and actual elevation using a lapse rate 7.2 K km^{-1}.

	Obs	RACMO2.3 5.5 km			
	Mean	Bias	σ_{bias}	RMSD	r^2
Arturo Prat	271.1	0.27	0.76	0.64	0.95
Bellingshausen	270.9	−0.51	0.56	0.54	0.97
Bonaparte Point	271.0	−0.06	1.43	1.25	0.82
Butler Island	256.5	−0.94	1.75	1.75	0.96
Esperanza	268.3	−0.52	1.04	0.83	0.97
Faraday/Vernadsky	270.2	−0.15	0.99	0.85	0.93
Larsen Ice Shelf	258.7	1.45	1.72	1.10	0.98
Limbert	250.5	0.15	1.32	1.25	0.98
Marambio	264.9	0.18	1.63	1.28	0.94
O'Higgins	269.6	−0.71	0.74	0.71	0.96
Rothera	268.9	−0.02	1.22	0.97	0.94
San Martin	268.8	0.02	1.73	1.36	0.90

Figure 3 compares the observed and modeled seasonal cycle and interannual variability of monthly mean 2-m temperatures at the 12 individual stations that are used in this study. For the northern and western stations (Figs. 3a,b,c,e,f,i,j,k,l), summer temperatures are underestimated, likely as a result of the stations being located on or near ice- and snow-free rock outcrops, while RACMO2.3 assumes continuous year-round snow/ice cover. As a result, model albedo is likely overestimated, and too much solar radiation is reflected. For these stations, winter temperatures match very well. The other stations (Figs. 3d,g,h) are located on the flat eastern ice shelves and are generally much colder in winter. The seasonality in 2-m temperature is captured well, in particular the "peaked" summer and the "coreless" winter, characteristic of East Antarctic temperature seasonality (Wendler et al. 1988). For the Larsen Ice Shelf station (Fig. 3g), an overestimation of winter temperature is seen; this could be related to overestimated wind speed warming the surface layer too much (see section 3c) or to the many missing winter measurements for this station and/or poor data quality caused by icing–riming that happens during relatively warm–moist winter episodes.

b. Trends in near-surface temperature

Figure 4 shows seasonal modeled $T_{2\,m}$ trends as a function of the observed trend for long-term (1979–2013) and short-term (decadal) periods (1981–90, 1991–2000, 2001–13). The observed trends are represented well by the model, especially in autumn and winter (r^2 = 0.83, 0.71), when warming rates are the largest and most significant, but uncertainties (one standard deviation; only plotted if significant >95%) are relatively large. We find that cooling trends predominantly stem from the last two decades, the 2001–13 period in particular, not showing a clear seasonality and is present both in the eastern and the western AP stations. Because of limited observation lengths, no long-term trend could be calculated for the eastern ice shelf stations, and trends shown are mostly from the 2001–13 period.

c. Near-surface wind speed

Figure 5 shows modeled versus observed average (1979–2013), yearly averaged and monthly 10-m wind speed ($V_{10\,m}$), and average (1979–2013) 10-m wind direction at the 12 SCAR-READER stations. The stations show a broad range of 10-m wind speeds: annual average $V_{10\,m}$ ranges from 3 to 8 m s^{-1}, while interannual variability (one standard deviation, expressed as error bars) also varies somewhat among the stations, which is partly because of different observation lengths. Wind directions are mostly westerly, except for Rothera and San Martin, which experience northerly flow. Wind direction is represented well by the model, except for Faraday/Vernadsky. The scatter in monthly $V_{10\,m}$ is relatively large (r^2 = 0.5), but the bias is small (0.18 m s^{-1}). The coefficient of determination of the individual stations (Table 3) ranges from 0.2 to 0.7, where lower values are mostly for stations with shorter and incomplete records. Apart from model errors, discrepancies are caused by the difficulty of representing the rough terrain in which the stations are located at 5.5-km spatial resolution. This is especially the case for Bellingshausen and Arturo Prat, located on the South Shetland Islands (SSI), where biases in wind speed are large, probably as a result of poor representation of these islands in the model DEM. For all other stations, there is a slight tendency for low wind speeds to be overestimated and high wind speeds to be underestimated; this is caused by the still-limited horizontal resolution compared to the locally complex terrain and the fact that katabatic forcing is important for the near-surface wind climate. Apparently, as was the case for RACMO2.3 at 27 km (Van Wessem et al. 2014a), there is too much katabatic forcing for stations located in relatively flat terrain (i.e., LIS) and too little for stations located in steep terrain (i.e., most stations in the western AP), although the effect should be smaller at the resolution presented in this study.

Figure 6 compares the observed and modeled seasonal cycle and interannual variability of 10-m wind speed at the 12 individual stations. Seasonality in wind speed is represented relatively well by RACMO2.3 for most stations, but the variability

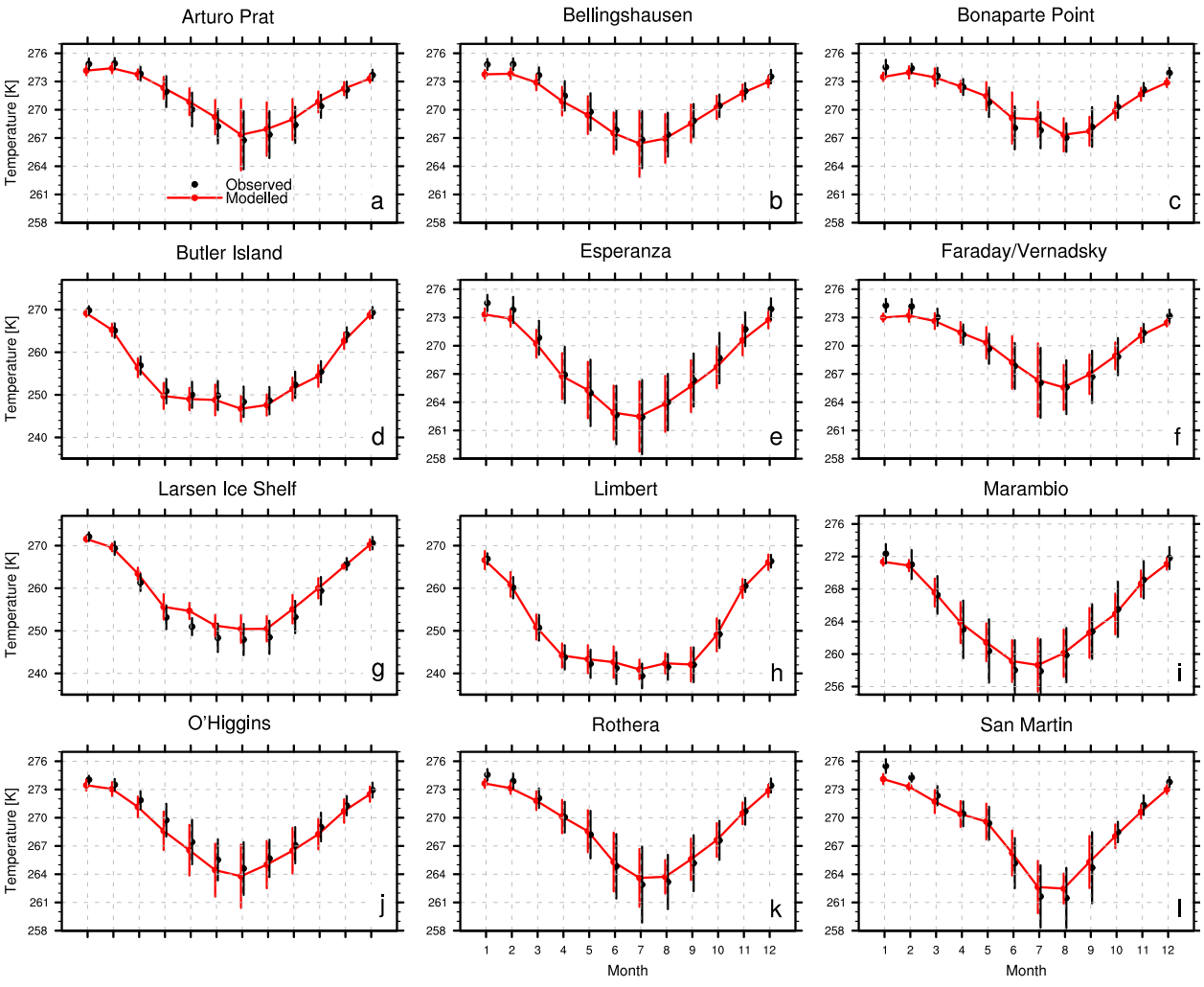

FIG. 3. Monthly average 2-m temperature $T_{2\,\mathrm{m}}$ for SCAR-READER stations (black dots) and RACMO2.3 (red lines). Error bars denote observed interannual variability of the respective month (1σ). Data for a particular month are only used when both the model and the observational data are available for that month. Modeled temperature is corrected for elevation differences between model and observations using a lapse rate of 7.2 K km^{-1}. Information about the stations can be found in Table 1.

(represented by the error bars) is generally less than in the observations. The largest bias is seen for the Larsen Ice Shelf in winter. Apart from model errors, this might be partly explained, as with temperature, by sensor problems such as icing/riming, as suggested by the frequently missing winter observations for this station.

Figure 7 shows that the generally weak seasonal cycle in wind direction at most stations is simulated well for most stations, except for Faraday, although wind speed at this station is well simulated. This suggests that, at this location, the direction of the slope is poorly resolved, which is likely because of the station being located on a small island. At the ice shelf stations Larsen C and Limbert, the strong wind direction seasonality is caught particularly well.

d. Vertical profiles of temperature and wind

Figure 8 presents RACMO2.3, ERA-Interim, and observed average (2002–13) upper-air temperature, wind speed, and wind direction for three SCAR-READER stations. RACMO2.3 and ERA-Interim correctly resolve the temperature profile at all stations. The model simulates the winds well for the lower atmosphere, but at higher levels in the atmosphere, modeled and observed wind speed slightly deviate, which, apart from model errors, may be partly related to the horizontal advection of the balloons. The westerly wind direction in the upper atmosphere and, especially at Rothera, the turning toward more northerly lower-atmosphere winds is represented well by the model; this effect is absent in ERA-Interim,

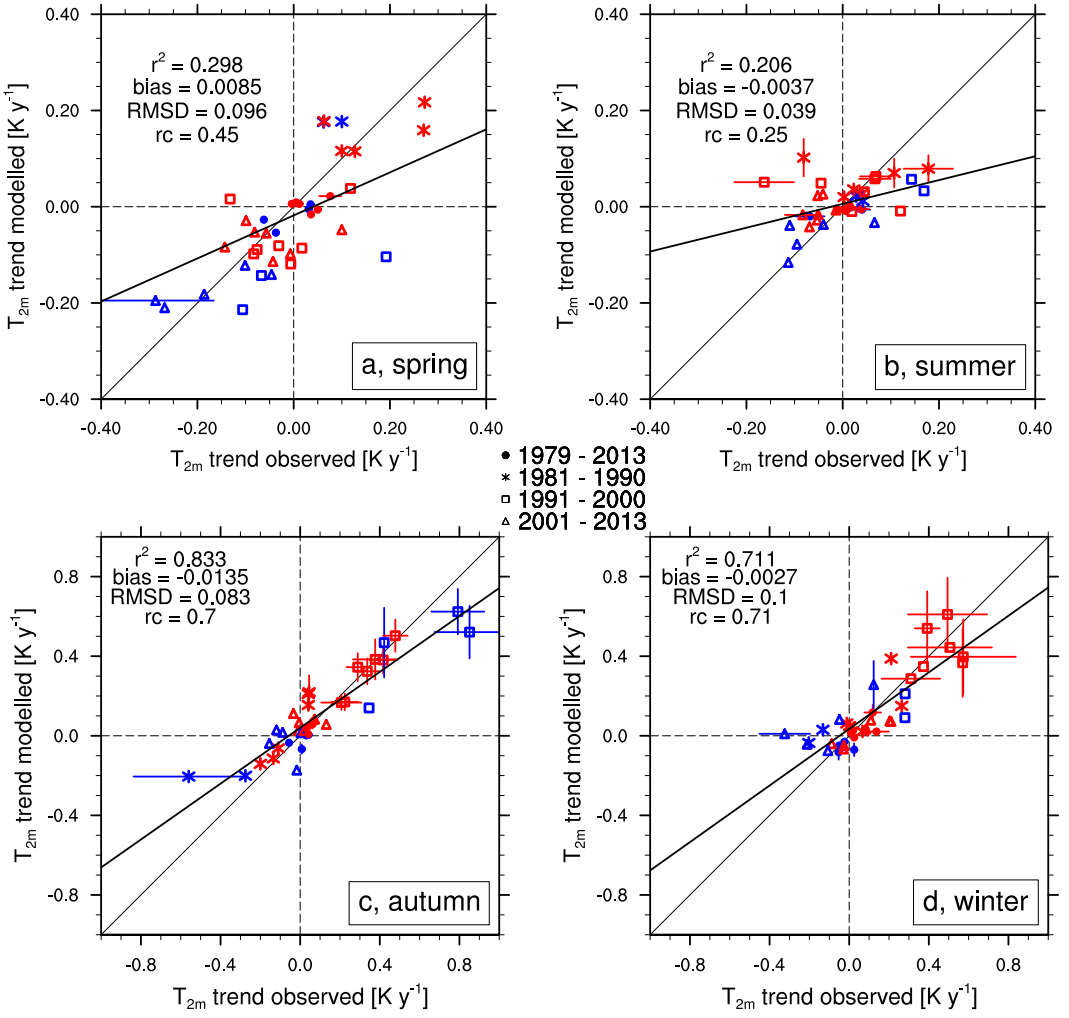

FIG. 4. Modeled vs observed (a) spring, (b) summer, (c) autumn, and (d) winter trends in $T_{2\,\mathrm{m}}$ ($\mathrm{K\,yr^{-1}}$) for 1979–2013 (circles), 1981–90 (asterisks), 1991–2000 (squares), and 2001–13 (triangles). Error bars show 1σ deviations of the calculated trend (only if significant at >95%). Trends are not shown if insufficient observational data are available (<50% of the respective period). SCAR-READER stations situated in the eastern AP are denoted in blue (Esperanza, Marambio, Larsen Ice Shelf, Butler Island, and Limbert). Coefficients of determination r^2, bias, RMSD, and regression slope (rc) of all trends are shown; regression lines are based on all trends. Note the different axes for the bottom panels.

showing the additional value of RACMO2.3 over ERA-Interim.

We use two balloon soundings from 11 January and 23 January 2011 performed simultaneously east and west of the AP at the locations of Rothera and AWS 14 on the Larsen C Ice Shelf to evaluate modeled gradients across the AP mountains. These dates represent two very different meteorological situations, with a strong low pressure system to the east of the AP on 11 January (Fig. 9a) and to the west of the AP on 23 January (Fig. 9b). To the east of the AP, 11 January, cold air is advected from the south along the mountain range by the large-scale circulation. The wind speed maximum close to the surface represents a barrier wind jet, which is a phenomenon frequently observed in the eastern AP (Schwerdtfeger 1975; Parish 1983). It is formed by cold air, advected from the southeast, piling up against the AP mountains creating a pressure gradient that forces a cold southerly flow. RACMO2.3 simulates the characteristic temperature and wind profiles well, although the wind speed in the jet is overestimated. At AWS 14, the inversion in temperature at ~1000 m is also simulated well. RACMO2.3 accurately simulates the weaker upper-air winds and their predominantly southerly direction.

Figure 9b shows the conditions for 23 January 2011, with northerly large-scale winds. Warm air is now advected toward the AP, which is reflected in the higher temperatures when compared to 11 January. RACMO2.3

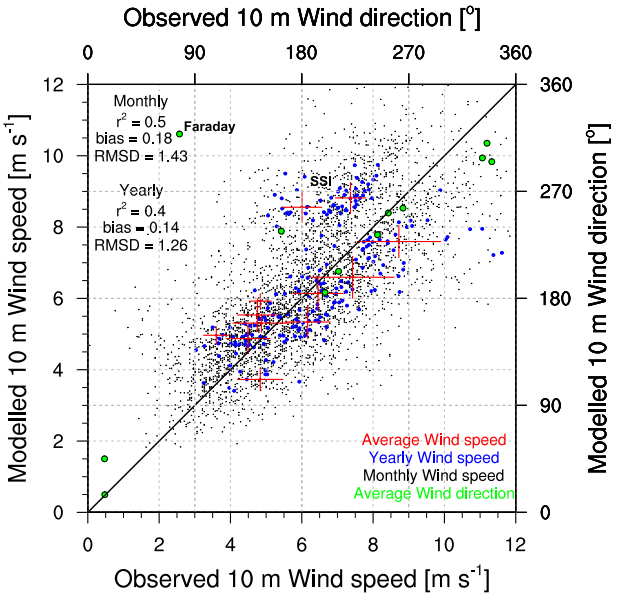

FIG. 5. As in Fig. 3, but for 10-m wind speed $V_{10\,m}$ ($m\,s^{-1}$) and 1979–2013 average wind direction (green, right axis) (°). SSI denotes the two South Shetland Island stations.

resolves the temperature profile with reasonable precision, although the inversion at 2000 m is not sufficiently pronounced. The profiles for wind speed/direction also show reasonable correspondence, especially for wind direction. The observed wind speed profile at Rothera shows larger variability with height than the model. Apart from model errors, this mismatch is likely a combination of multiple effects that complicate a correction of the data and, thus, a direct comparison: it is related to the mismatch of model and the actual topography, the horizontal displacement of the balloon, and the radiosonde measurements being performed over a longer time period than the (instantaneous) model output.

e. *Effects of horizontal resolution*

For the same day as in Fig. 9a, Fig. 10 shows the daily average (11 January 2011) 10-m wind speed and 2-m temperature of RACMO2.3 at 5.5 km and of ERA-Interim at ~80-km horizontal resolution. In addition, Figs. 11, 12, 13, 14, and 15 show ERA-Interim climate maps next to the RACMO2.3 climate maps, all illustrating the added value of the high-resolution results over the ERA-Interim fields. The high resolution has a significant impact on simulated winds in rough terrain, which has been previously discussed in Bromwich et al. (2005) and Lenaerts et al. (2012b), which focused on other regions in Antarctica. At 5.5 km, more detail and more pronounced temperature and wind speed gradients are simulated over the AP mountain range. Moreover,

TABLE 3. As in Table 2, but for 10-m wind speeds $V_{10\,m}$ ($m\,s^{-1}$).

	Obs Mean	RACMO2.3 5.5 km			
		Bias	σ_{bias}	RMSD	r^2
Arturo Prat	6.0	2.64	1.25	1.07	0.36
Bellingshausen	7.4	1.45	0.72	0.72	0.68
Bonaparte Point	4.8	0.99	1.03	0.92	0.50
Butler Island	4.9	0.40	0.75	0.61	0.66
Esperanza	7.4	−0.81	1.44	1.22	0.53
Faraday/Vernadsky	4.5	0.37	0.90	0.81	0.55
Larsen Ice Shelf	3.6	1.32	0.90	0.69	0.21
Limbert	4.8	0.99	0.92	0.78	0.37
Marambio	8.7	−1.1	1.31	0.93	0.59
O'Higgins	6.5	−0.24	1.53	1.10	0.19
Rothera	6.2	−0.83	0.79	0.72	0.72
San Martin	4.8	−1.09	1.31	0.71	0.32

local features, such as wind and temperature over the George VI Ice Shelf or the strong downslope winds on the southeastern slopes, are now resolved. Also, note the strong wind speed gradient over the Larsen C Ice Shelf.

4. Results: Climate of the Antarctic Peninsula

In this section, we discuss the Antarctic Peninsula climate in terms of upper-atmosphere and near-surface wind and temperature, their seasonality, and spatial and interannual variability.

a. *Seasonality*

Figures 11a,b show the RACMO2.3 and ERA-Interim climatological average (1979–2013) large-scale circulation and geopotential height pattern at 700 hPa. The Antarctic Peninsula climate is characterized by persistent upper-air westerly winds that advect warm and moist southern Pacific Ocean air toward the AP. The strong resemblance of the RACMO2.3 and ERA-Interim circulation patterns shows that the simulation is strongly constrained by the lateral boundaries and that much of the good model performance at these scales comes from the quality of the reanalysis. Figure 12a shows that the westerly winds are notably weaker in summer than in winter (Fig. 12b), following the seasonal variations in the depth of the circumpolar pressure trough. West of the AP mountain ridge, which peaks at elevations of 2500 m above sea level, the upper-air winds are deflected toward the south, especially in summer, transporting relatively warm and moist maritime air to the ice sheet. In winter, winds are more zonal.

The strong upper-air westerlies are only partly reflected in the near-surface (10 m) winds (Figs. 11c,d), where there are significant differences between RACMO2.3 and the reanalysis over the ice sheet

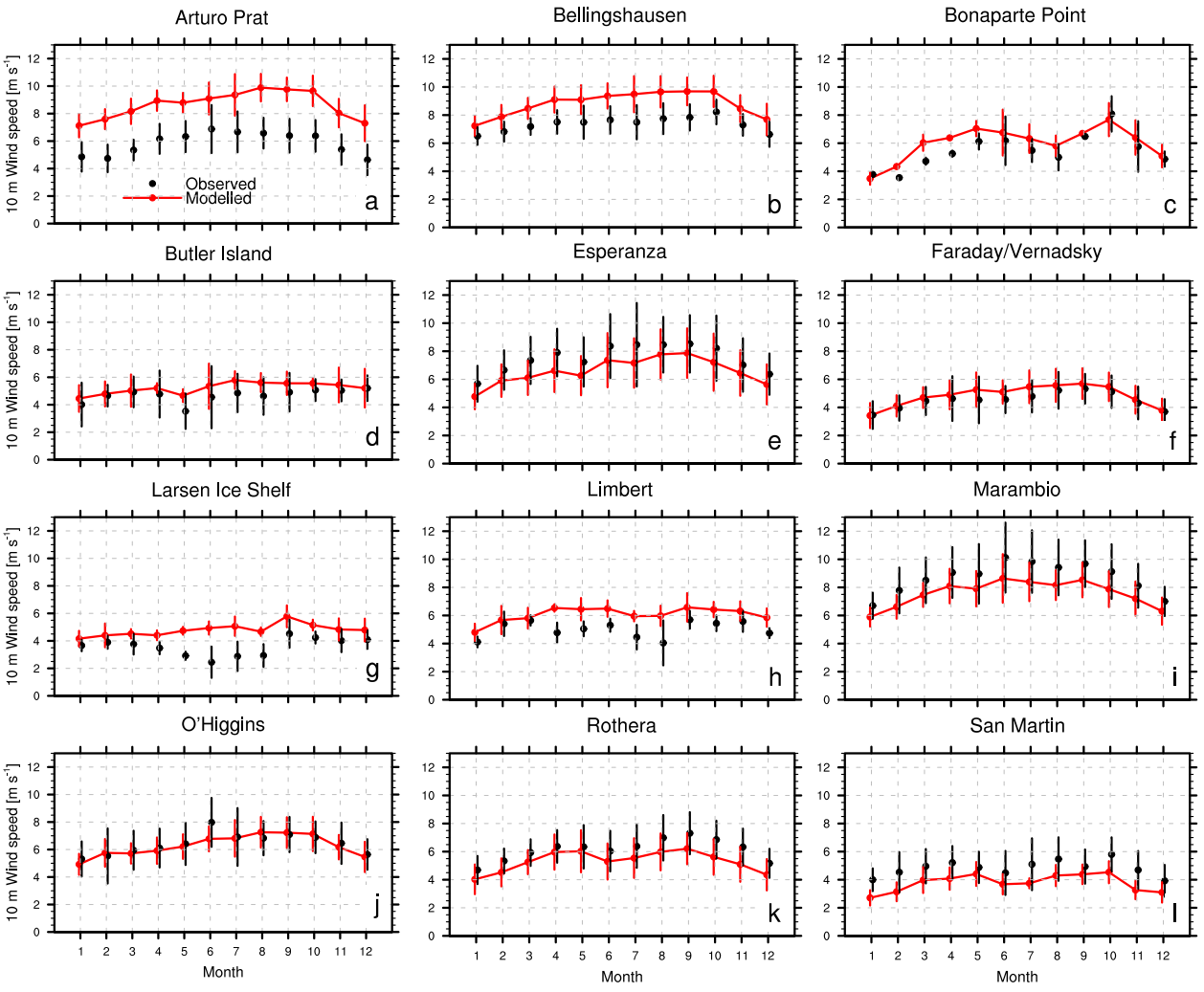

FIG. 6. As in Fig. 3, but for 10-m wind speed $V_{10\,\mathrm{m}}$.

topography. In summer, near-surface winds over the ocean are largely blocked by the mountain range: west of the AP, the winds veer toward the south, following the topography, but are relatively weak (Orr et al. 2008). In winter (Fig. 12c), winds are stronger over the southwestern slopes because of katabatic wind forcing. This is especially true toward the southwest, where slopes are more extensive and clouds are less persistent, resulting in more longwave cooling of the surface: here, annual mean $V_{10\,\mathrm{m}}$ reaches values $>10\,\mathrm{m\,s^{-1}}$. To the east of the AP, winds are mostly southerly, following the AP orography, advecting cold air from the south. These are the well-known AP barrier winds, caused by the interaction between cold air from the Filchner Ronne Ice Shelf, the ice-covered Weddell Sea, and the AP mountains (Schwerdtfeger 1975; Parish 1983).

The AP near-surface (2 m) temperature, shown in Figs. 11e,f and 12e,f, is closely related to elevation, latitude, and circulation: average (1979–2013) $T_{2\,\mathrm{m}}$ decreases from ~270 K along the northwestern coastline to ~250 K at the top of the spine in the southern AP. Note the wintertime relative maxima in $T_{2\,\mathrm{m}}$ over the lower slopes of the mountain range, indicative of katabatic winds that enhance sensible heat transport toward the surface (Van den Broeke et al. 1999). This feature is strongest in winter when temperatures over the flat ice shelves are, in the absence of katabatic flow, lower than over the nearby slopes. The large (~10 K) wintertime east–west temperature gradient over the AP is caused by the advection of cold air by southerly winds to the east of the AP and the advection of warmer air by northerly winds in the west of the AP. These differences are further enhanced by the ensuing differences in sea ice cover, with sea ice cover being more extensive in the Weddell Sea to the east of the AP.

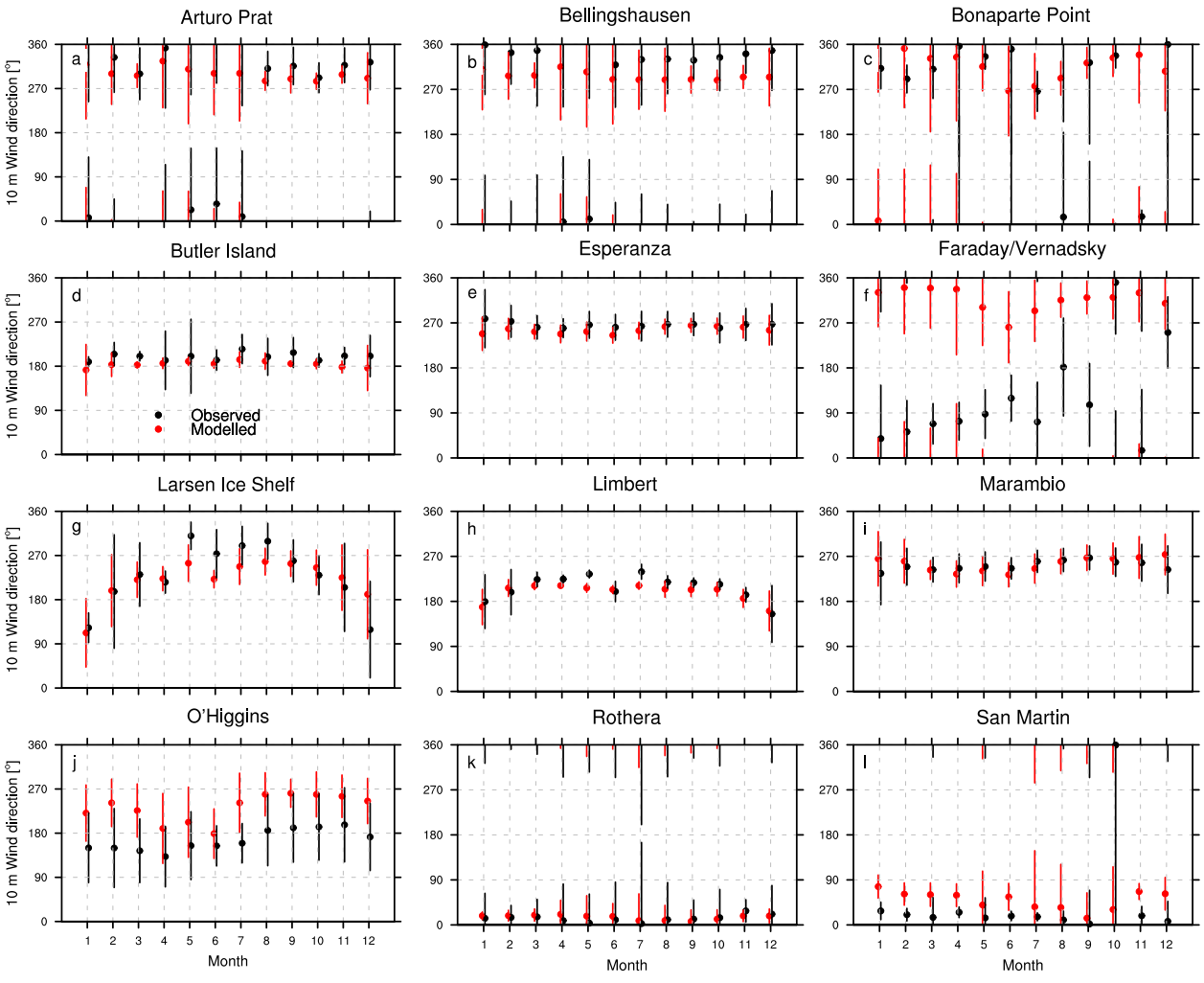

FIG. 7. As in Fig. 6, but for wind direction (°). Wind direction and standard deviation are calculated from monthly vector means.

b. *Variability*

Figure 13a shows there is low interannual variability of $T_{2\,\mathrm{m}}$ for the western AP and high interannual variability for the eastern slopes of the AP. This is probably associated with the presence of a layer of cold air in the east, its variable depth causing variable thermal winds opposing the katabatic winds (Van Angelen et al. 2011), as well as lee slope effects of the variability in westerly atmospheric circulation; these effects are not caught in the low-resolution dataset (Fig. 13b). On the ice shelves, wind speed variability is low in the absence of katabatic forcing.

Figures 13c,d show that directional constancy (DC; the ratio of absolute and vector mean wind speed) is high over the AP slopes, where katabatic forcing is strongest. In the northwest, where katabatic winds oppose the relatively strong large-scale circulation, DC is lower. Over the flat ice shelves, DC is also relatively low in the absence of katabatic forcing; here, conditions are mostly influenced by varying large-scale/mesoscale pressure gradients. Over the Ronne Ice Shelf toward the AP mountain range, a barrier wind signature is visible with locally higher DC values. Particularly interesting and counterintuitive are the high DC values over the northeastern AP mountain slopes, while simultaneously the interannual variability of $V_{10\,\mathrm{m}}$ on these slopes is high. This indicates high variability in wind speed but low variability in wind direction. It is likely that, over the eastern AP slopes, variable barrier winds, in combination with synoptically forced foehn winds (Elvidge et al. 2014), influence the wind strength over the slopes, which affects the magnitude of the wind but not its direction.

The impact of katabatic winds on sensible heat exchange and temperature is clearly illustrated in Fig. 14c: over the flat ice shelves, a strong surface-based temperature inversion is

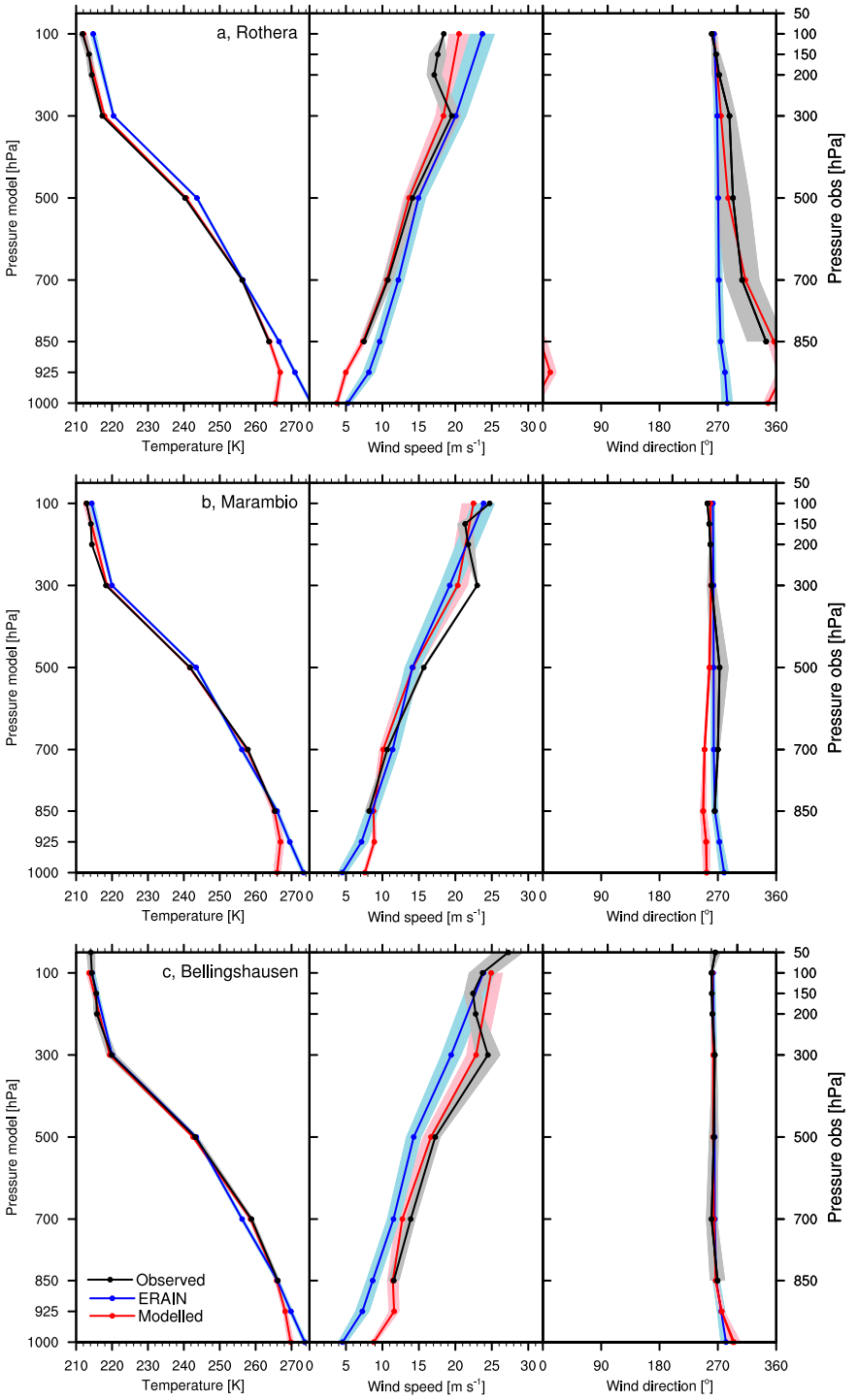

FIG. 8. The 2002–13 average profiles of observed balloon soundings (black lines), modeled (red) and ERA-Interim (blue) of (left to right) temperature, wind speed, and wind direction at (a) Rothera, (b) Marambio, and (c) Bellingshausen. Shading represents interannual variability (1σ).

able to develop, especially in winter. This inversion is weaker over the mountain slopes, where katabatic winds and hence downward mixing of warm air are strongest, resulting in higher potential temperatures, which is more clearly seen in the high-resolution data than in ERA-Interim (Fig. 14d). Locations with strong surface-based temperature inversions are also susceptible to strong warming when the inversion breaks up (e.g., because of

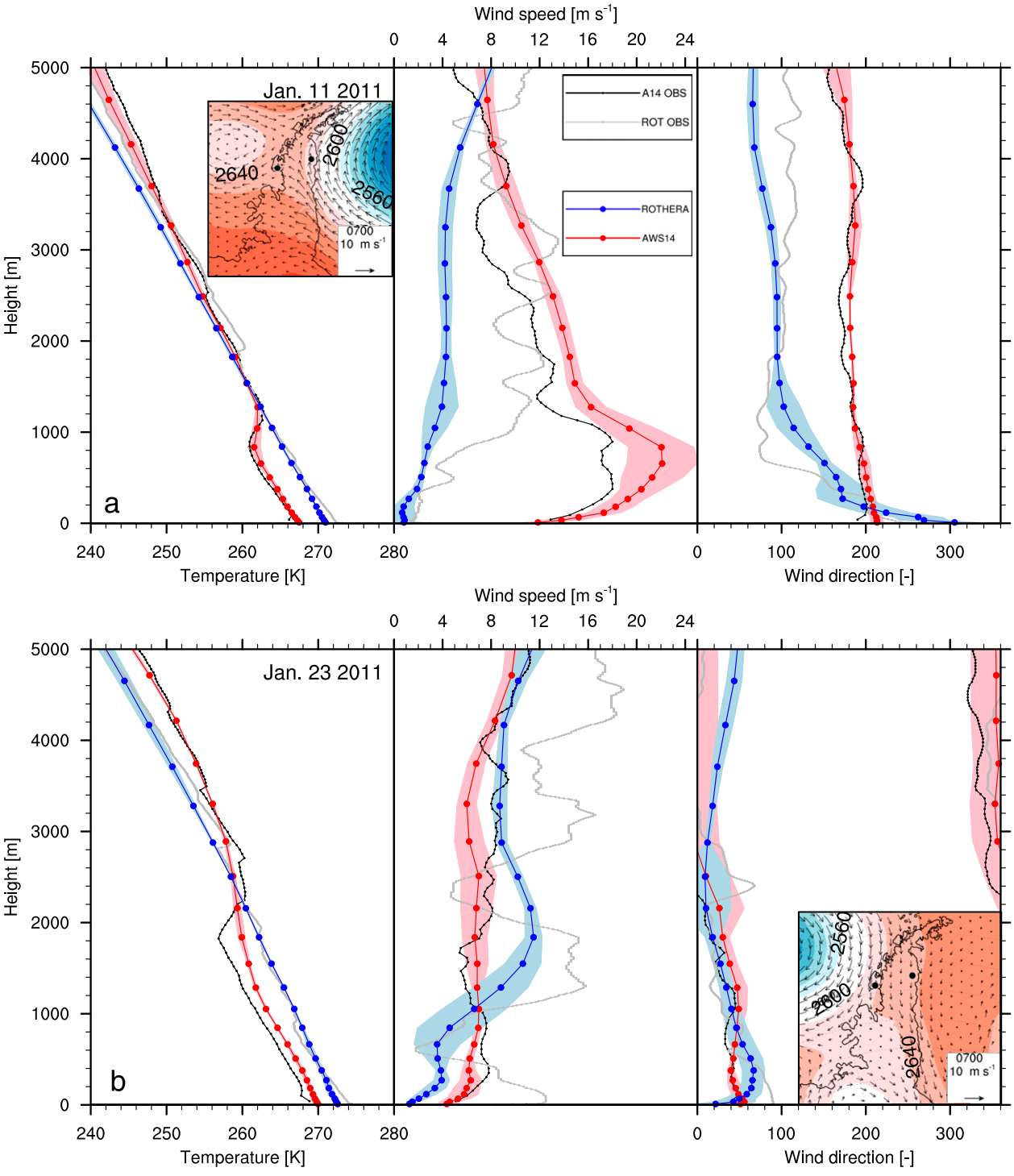

FIG. 9. Observed (balloon soundings; black and gray lines) and modeled (red and blue lines) profiles of (left to right) temperature, wind speed, and wind direction for (a) 11 Jan and (b) 23 Jan 2011. Insets show radiosonde locations (black dots) and 700-hPa winds (vectors) and geopotential height (m; contours). Shading of modeled profiles denotes 1σ based on 1200 UTC $\pm$ 3 h (5 modeled profiles).

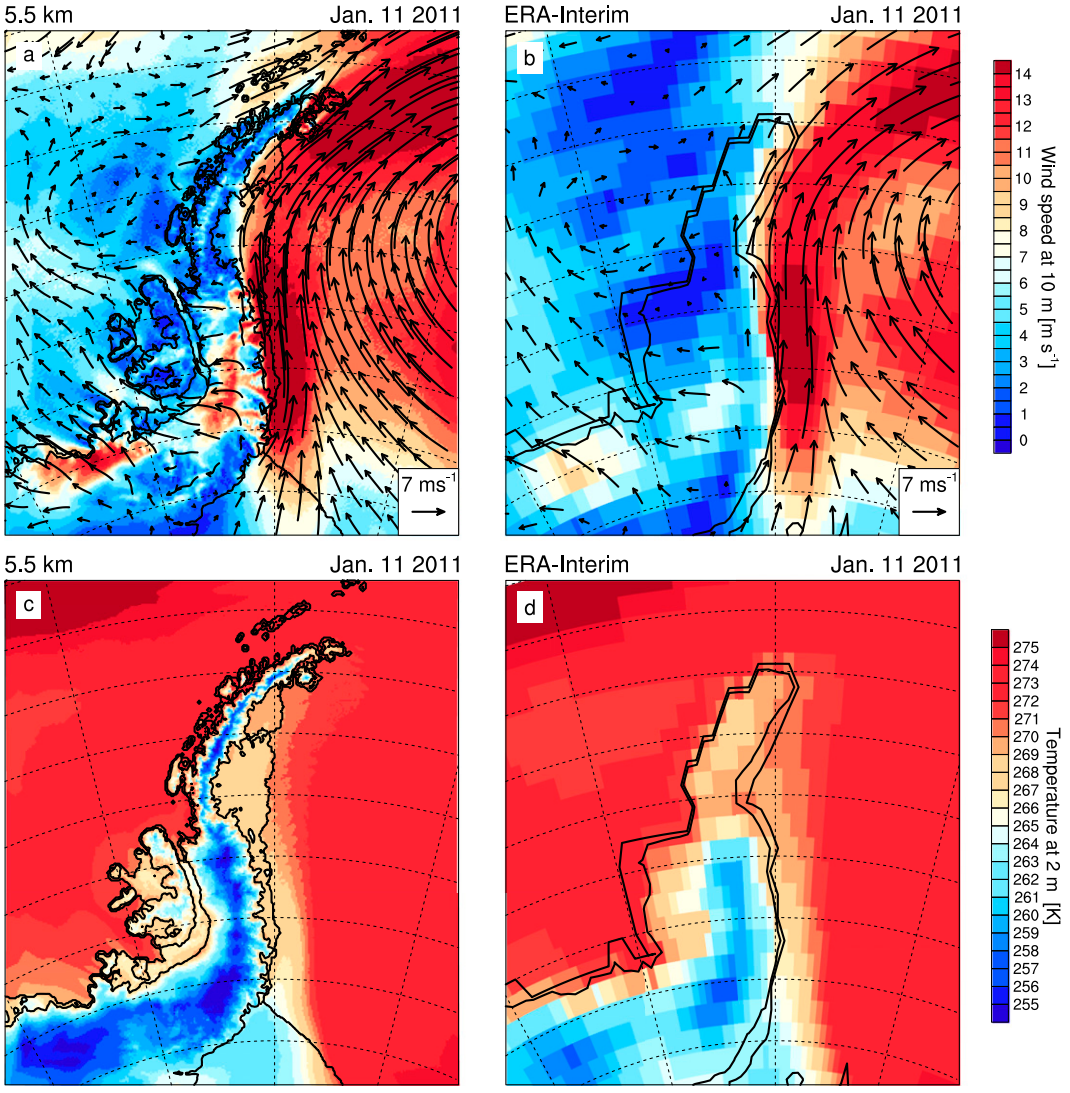

FIG. 10. (left) RACMO2.3 and (right) ERA-Interim daily mean (a),(b) 10-m wind speed $V_{10\,\mathrm{m}}$(vectors and contours) and (c),(d) 2-m temperature $T_{2\,\mathrm{m}}$ for 11 Jan 2011. Black contour lines represent the ice shelf edge and 100-m surface elevation. Vectors are plotted every three grid boxes to not obscure the plot.

clouds and winds warming the surface), enhancing temporal variability. This explains the patterns seen over the AP in Figs. 14a,b, where $T_{2\,\mathrm{m}}$ variability is low in regions where $\theta_{2\,\mathrm{m}}$ is high, and variability is high in regions where $\theta_{2\,\mathrm{m}}$ is low. Over the ocean, variability in $T_{2\,\mathrm{m}}$ is mostly determined by variability in sea ice cover. For instance, the area with a local minimum in the Weddell Sea is characterized by a semipermanent sea ice cover.

c. *Trends*

Figure 15a shows the modeled 1979–2013 trend of 2-m temperature. A warming occurred in the northwest of the AP and over the adjacent oceans of up to $\sim 0.05\,\mathrm{K\,yr^{-1}}$, which is significant at the >95% level near the mountain range. Over most of the AP, but especially over the east and the south, there has been significant cooling of up to $\sim 0.03\,\mathrm{K\,yr^{-1}}$, which has mostly occurred in the last decade (2001–13, not shown). This notable distinction between western AP warming and eastern AP cooling is closely related to the changes in the near-surface winds (Fig. 15b). Over the western AP, northerly winds have increased in strength. Over the eastern AP, enhanced barrier winds over the Ronne Ice Shelf have led to enhanced southerly winds near the surface and a decreased magnitude of the katabatic winds down the eastern AP slopes. These southerly winds increased the transport of cold air over the sea ice and Ronne Ice Shelf toward the northern AP ice shelves, leading to the cooling in this region.

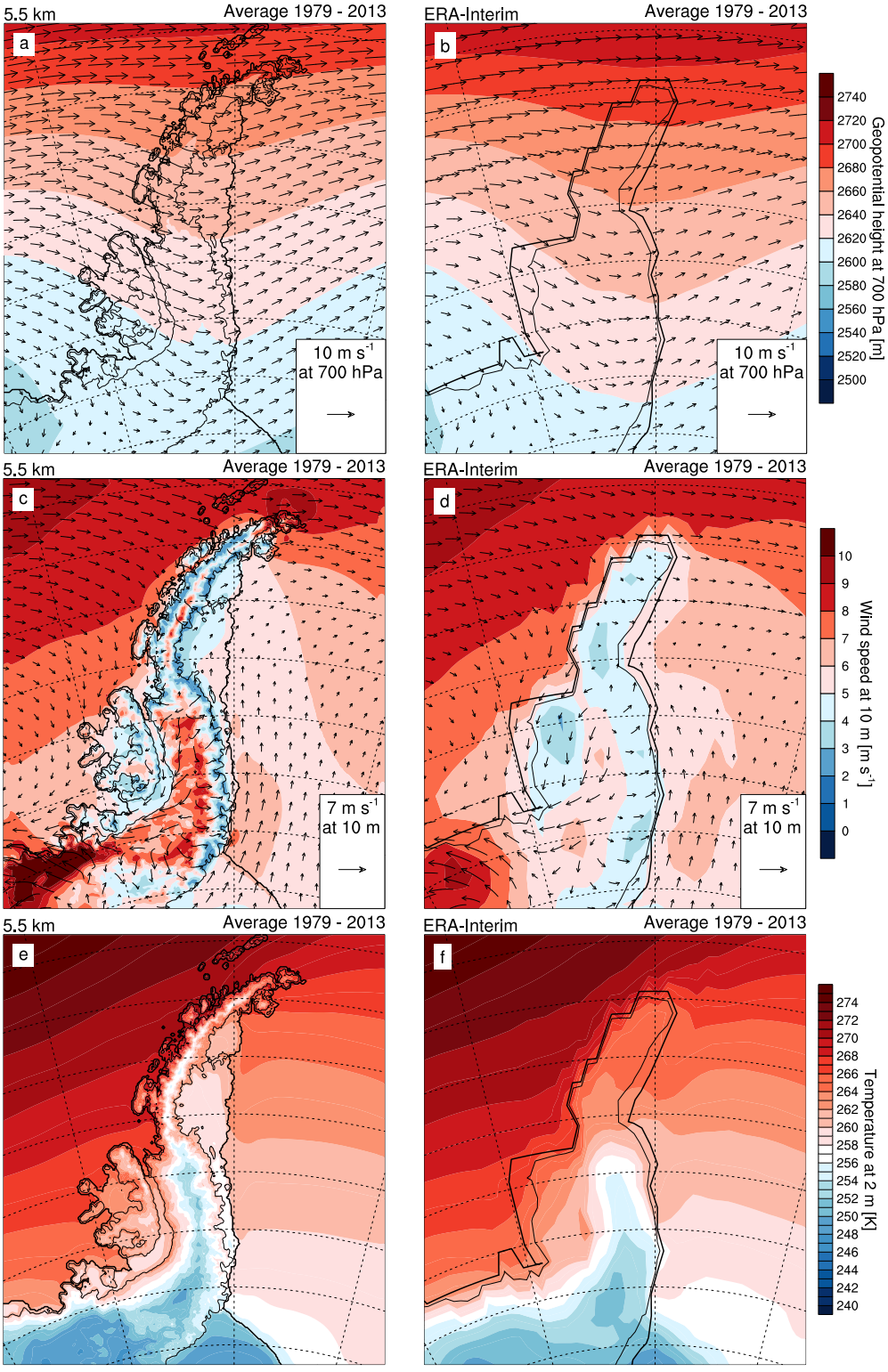

FIG. 11. (left) RACMO2.3 and (right) ERA-Interim 1979–2013 average (a),(b) 700-hPa geopotential height (colors) and wind speed vectors, (c),(d) 10-m wind speed (colors) and vectors, and (f),(g) 2-m temperature (colors). Black contour lines represent the ice shelf edge and 100-m surface elevation.

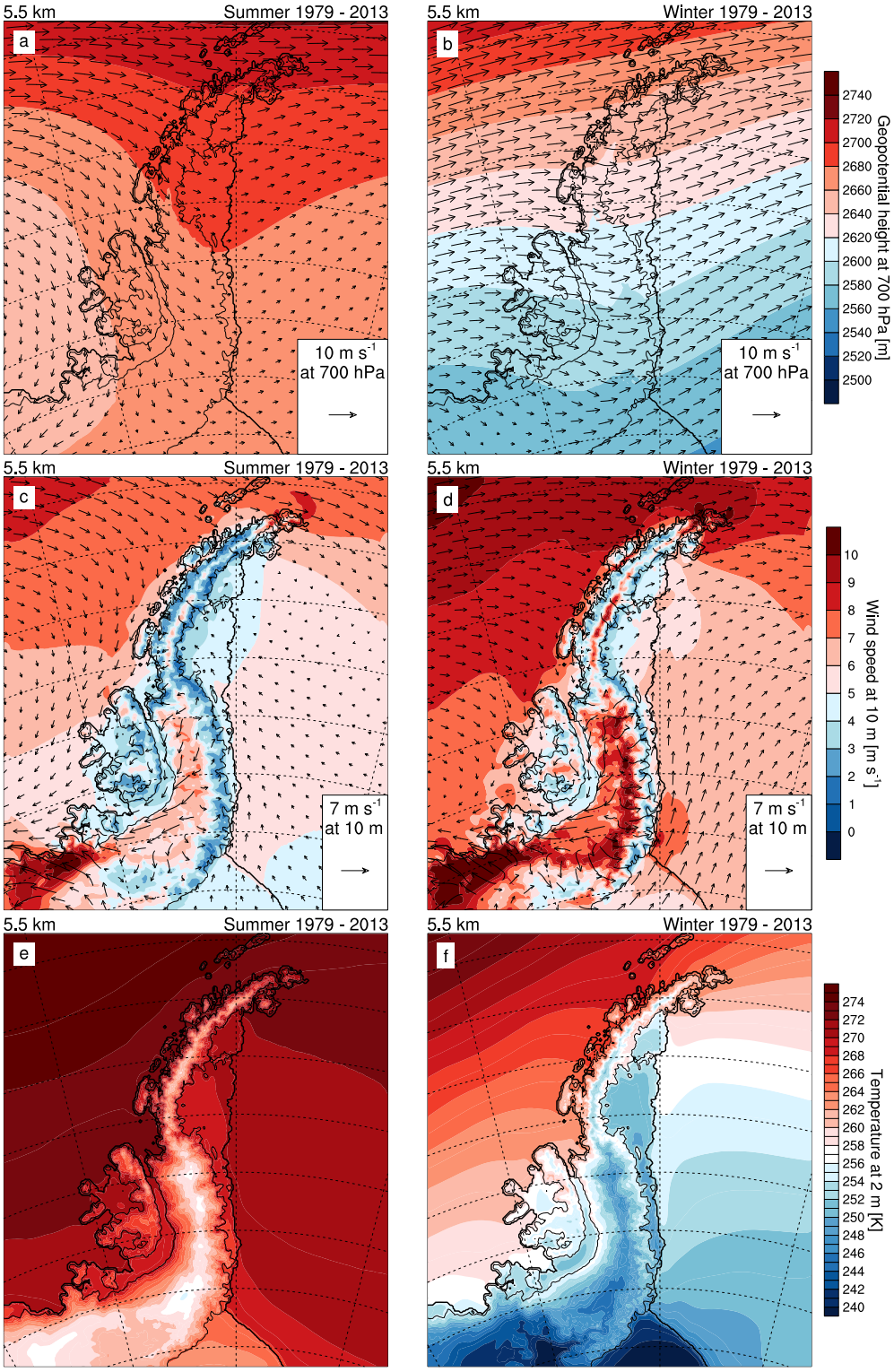

FIG. 12. RACMO2.3 (left) summer and (right) winter (1979–2013) (a),(b) 700-hPa geopotential height (colors) and wind speed vectors, (c),(d) 10-m wind speed (colors) and vectors, and (f),(g) 2-m temperature (colors). Black contour lines represent the ice shelf edge and 100-m surface elevation.

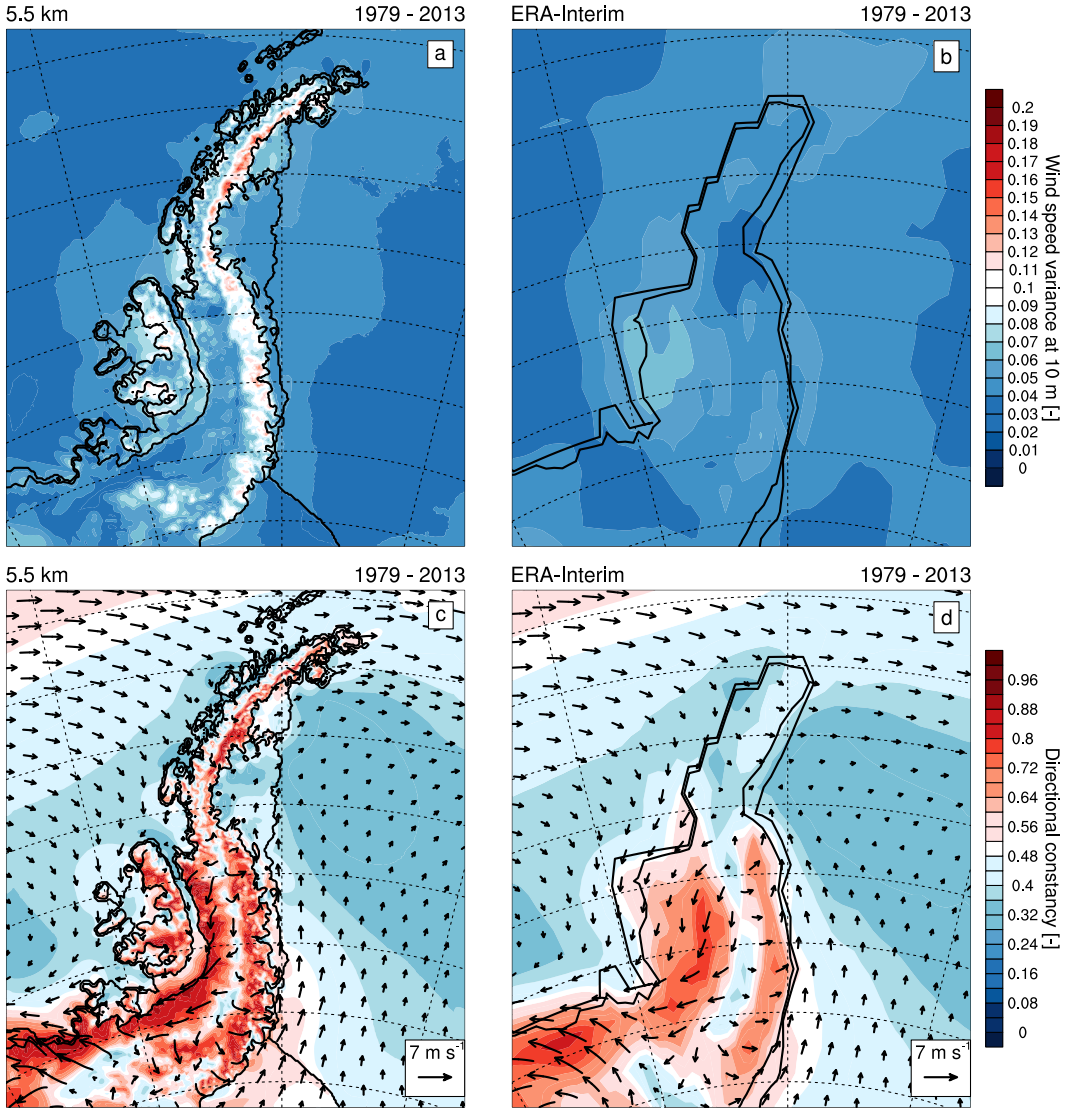

FIG. 13. (left) RACMO2.3 and (right) ERA-Interim interannual (1979–2013) variability (1σ; detrended and determined from yearly averages) of (a),(b) 10-m wind speed $V_{10\,\mathrm{m}}$, and (c),(d) directional constancy (DC). Wind speed variance is presented as a fraction of the mean wind speed. Black contour lines represent the ice shelf edge and 100-m surface elevation.

This clear west-to-east distinction in trends and features such as the seasonality, where over the western AP most warming occurs in winter, while for the eastern AP the warming is found in summer–autumn, are also found in ERA-Interim (Figs. 15b,d) and the SCAR-READER stations (Fig. 4) and have been previously reported using lower-resolution datasets (Bromwich 2004; Bracegirdle and Marshall 2012). However, the significant warming for the southwestern AP ice sheet in the low-resolution ERA-Interim dataset is not seen at 5.5 km, which rather shows a cooling.

These changes in near-surface wind speed and direction are also related to changes in sea ice fraction (Holland 2014). Figure 15e shows a significant decrease in sea ice to the west of the AP, which has further enhanced the warming in the western AP, especially in autumn and winter, when the retreat in sea ice is strongest (in summer this region is nearly free of sea ice). Over the Weddell Sea, the sea ice cover has increased near the front of the Larsen C and Larsen D Ice Shelves, possibly in response to enhanced flow from the south. Maps of decadal temperature trends (not shown) and Fig. 4 confirm that the long-term cooling signal in Fig. 15a stems mainly from the last decade in spring and summer; the other decades (in particular, 1991–2000) mostly show a warming signature,

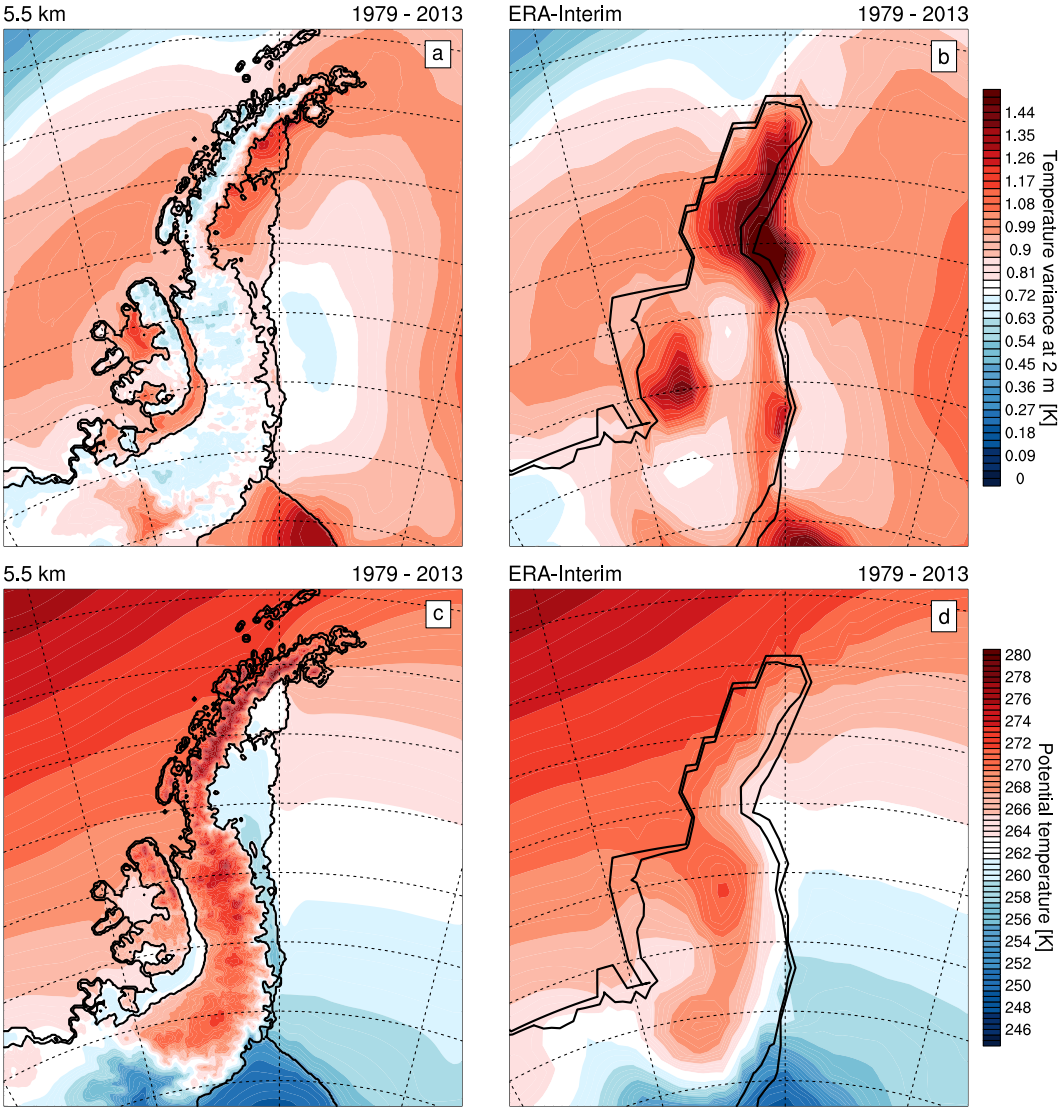

FIG. 14. As in Fig. 13, but for (a),(b) 2-m temperature and (c),(d) 2-m potential temperature.

which was also discussed by Bromwich and Fogt (2004) and Turner et al. (2005).

5. Summary and conclusions

We present and discuss the near-surface temperature and wind climate of the Antarctic Peninsula (AP) for 1979–2013, as simulated by the Regional Atmospheric Climate Model, version 2.3 (RACMO2.3), at a relatively high horizontal resolution of 5.5 km. The model is forced by ERA-Interim data at the lateral boundaries and includes an updated model surface topography. We evaluate model performance by comparing output to temperature and wind measurements from 12 manned and automatic weather stations in the SCAR-READER dataset and vertical profiles of temperature and wind from balloon soundings. The seasonal cycle in temperature is simulated well, although summer temperatures are slightly underestimated at the western AP stations, probably as a result of an overestimated summer (rock vs snow surface) albedo near the stations. The winter temperature at most stations is represented well, including the coreless winter at the ice shelf stations and the peaked winter for the warmer (western) coastal stations. In general, the model simulates wind speed/direction fairly well in terms of temporal and spatial variability, but considerable biases are found as a result of the model not adequately resolving the complex terrain in which the stations are situated, even at 5.5-km horizontal resolution. RACMO2.3 vertical profiles of temperature and wind at a daily scale are simulated relatively well, as a comparison with balloon soundings

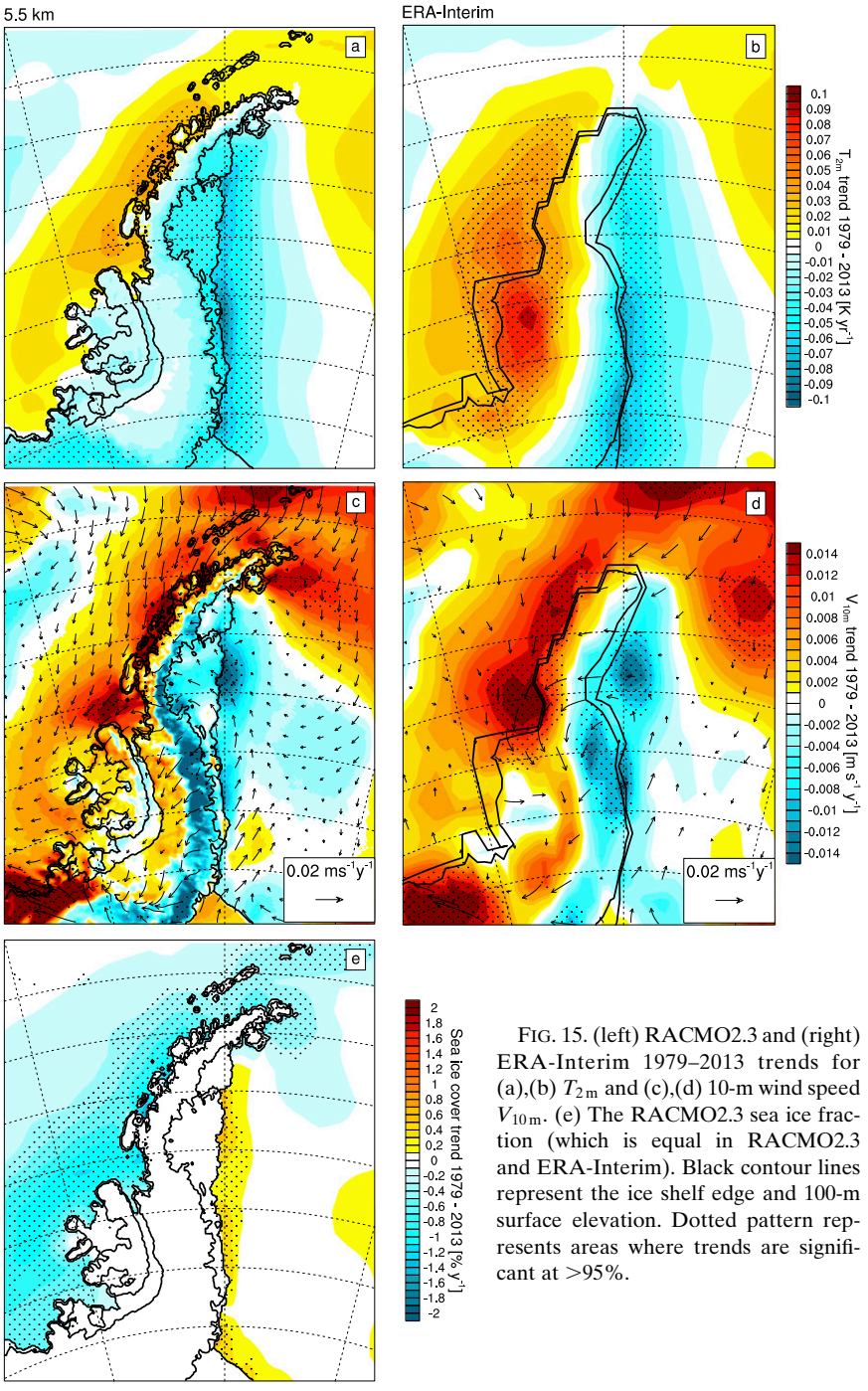

FIG. 15. (left) RACMO2.3 and (right) ERA-Interim 1979–2013 trends for (a),(b) $T_{2\mathrm{m}}$ and (c),(d) 10-m wind speed $V_{10\mathrm{m}}$. (e) The RACMO2.3 sea ice fraction (which is equal in RACMO2.3 and ERA-Interim). Black contour lines represent the ice shelf edge and 100-m surface elevation. Dotted pattern represents areas where trends are significant at >95%.

shows, but because of both measurement and model uncertainties, there are also important discrepancies.

High-resolution AP climate maps of modeled near-surface temperature and wind show that winds and temperature have large spatial variability: over the steep and high mountain ranges of the northern AP, there are pronounced west-to-east climate gradients, while in the more gently sloping southern AP mountains, temperatures are low and wind is dominated by katabatic forcing. Over the ice shelves, in the absence of katabatic forcing, a strong surface-based temperature inversion develops, resulting in strong temporal variability in temperature. Katabatic wind forcing has a strong influence on the southern AP climate: here, the wind is mostly uniform in direction throughout the year, and the potential temperature is high because of enhanced vertical mixing in the surface layer. Over the

eastern AP slopes, katabatic winds interact with barrier winds, and wind speed is highly variable, but wind direction remains constant.

Maps of temperature trends for 1979–2013 show a statistically significant warming of the northwestern AP and statistically significant cooling of the eastern and southern AP, in agreement with observed trends from the SCAR-READER stations. The temperature trends are related to a complex interplay of changes in atmospheric circulation, near-surface winds and sea ice, letting more warm ocean air to be transported to the northwestern AP and more cold ice shelf air to be transported to the eastern AP.

In future research, in order to further improve model results, the effects of more dynamic ocean and sea ice models should be investigated. Currently, ocean temperature and sea ice fraction are prescribed from reanalysis data, and a constant sea ice thickness is used. Moreover, at 5.5 km and higher horizontal resolutions, the limit of the hydrostatic assumption likely is reached, and a nonhydrostatic model should be used and may further improve model results. However, nonhydrostatic physics are beyond the scope of the current configuration of RACMO2.3. Finally, there is an increasing necessity for using more realistic prognostic cloud physics, such as taking into account the horizontal advection of precipitation. Recent studies (e.g., Van Wessem et al. 2014a; King et al. 2015), as well as this study, have shown clouds and their interaction with high mountain ranges and detailed topography to be of prime importance for the Antarctic climate, and this is especially true in regions like the Antarctic Peninsula.

Acknowledgments. We are grateful for the financial support of NWO/ALW, Netherlands Polar Programme. We thank the ECMWF for the use of their supercomputing facilities. Graphics and calculations were made using the NCAR Command Language (Version 6.2.1; UCAR/NCAR/CISL/VETS 2014). We thank Peter Kuipers Munneke for providing us with the Larsen C Ice Shelf radiosonde data and Stefan Ligtenberg for providing us with the FDM data for model initialization. We are grateful for data from the SCAR-READER dataset and for Steve Colwell helping us with the usage of these data. We thank three anonymous reviewers for their helpful comments, which have improved the paper.

REFERENCES

Bamber, J., and J. Gomez-Dans, 2009: A new 1 km digital elevation model of the Antarctic derived from combined satellite radar and laser data—Part 1: Data and methods. *Cryosphere,* **3,** 101–111, doi:10.5194/tc-3-101-2009.

Barrand, N. E., D. G. Vaughan, N. Steiner, M. Tedesco, P. Kuipers Munneke, M. R. van den Broeke, and J. S. Hosking, 2013: Trends in Antarctic Peninsula surface melting conditions from observations and regional climate modeling. *J. Geophys. Res.: Earth Surf.,* **118,** 315–330, doi:10.1029/2012JF002559.

Bracegirdle, T. J., and G. J. Marshall, 2012: The reliability of Antarctic tropospheric pressure and temperature in the latest global reanalyses. *J. Climate,* **25,** 7138–7146, doi:10.1175/JCLI-D-11-00685.1.

Bromwich, D. H., 2004: Modeled Antarctic precipitation. Part I: Spatial and temporal variability. *J. Climate,* **17,** 427–448, doi:10.1175/1520-0442(2004)017<0427:MAPPIS>2.0.CO;2.

——, and R. L. Fogt, 2004: Strong trends in the skill of the ERA-40 and NCEP–NCAR reanalyses in the high and midlatitudes of the Southern Hemisphere, 1958–2001. *J. Climate,* **17,** 4603–4620, doi:10.1175/3241.1.

——, A. J. Monaghan, K. W. Manning, and J. G. Powers, 2005: Real-time forecasting for the Antarctic: An evaluation of the Antarctic Mesoscale Prediction System (AMPS). *Mon. Wea. Rev.,* **133,** 579–603, doi:10.1175/MWR-2881.1.

Cassano, J. J., and T. R. Parish, 2000: An analysis of the nonhydrostatic dynamics in numerically simulated Antarctic katabatic flows. *J. Atmos. Sci.,* **57,** 891–898, doi:10.1175/1520-0469(2000)057<0891:AAOTND>2.0.CO;2.

Claremar, B., F. Obleitner, C. Reijmer, V. Pohjola, A. Waxegård, F. Karner, and A. Rutgersson, 2012: Applying a mesoscale atmospheric model to Svalbard glaciers. *Adv. Meteor.,* **2012,** 321649, doi:10.1155/2012/321649.

Cook, A. J., and D. G. Vaughan, 2010: Overview of areal changes of the ice shelves on the Antarctic Peninsula over the past 50 years. *Cryosphere,* **4,** 77–98, doi:10.5194/tc-4-77-2010.

——, T. Murray, A. Luckman, D. G. Vaughan, and N. E. Barrand, 2012: A new 100-m Digital Elevation Model of the Antarctic Peninsula derived from ASTER Global DEM: Methods and accuracy assessment. *Earth Syst. Sci. Data,* **4,** 129–142, doi:10.5194/essd-4-129-2012.

Dee, D. P., and Coauthors, 2011: The ERA-Interim reanalysis: Configuration and performance of the data assimilation system. *Quart. J. Roy. Meteor. Soc.,* **137,** 553–597, doi:10.1002/qj.828.

Elvidge, A. D., I. A. Renfrew, J. C. King, A. Orr, T. A. Lachlan-Cope, M. Weeks, and S. L. Gray, 2014: Foehn jets over the Larsen C Ice Shelf, Antarctica. *Quart. J. Roy. Meteor. Soc.,* **141,** 698–713, doi:10.1002/qj.2382.

Ettema, J., M. R. van den Broeke, E. van Meijgaard, W. J. van de Berg, J. E. Box, and K. Steffen, 2010: Climate of the Greenland ice sheet using a high-resolution climate model—Part 1: Evaluation. *Cryosphere,* **4,** 511–527, doi:10.5194/tc-4-511-2010.

Fettweis, X., 2007: Reconstruction of the 1979–2006 Greenland ice sheet surface mass balance using the regional climate model MAR. *Cryosphere,* **1,** 21–40, doi:10.5194/tc-1-21-2007.

Genthon, C., and G. Krinner, 2001: Antarctic surface mass balance and systematic biases in general circulation models. *J. Geophys. Res.,* **106,** 20 653–20 664, doi:10.1029/2001JD900136.

Holland, P. R., 2014: The seasonality of Antarctic sea ice trends. *Geophys. Res. Lett.,* **41,** 4230–4237, doi:10.1002/2014GL060172.

King, J. C., 1994: Recent climate variability in the vicinity of the Antarctic Peninsula. *Int. J. Climatol.,* **14,** 357–369, doi:10.1002/joc.3370140402.

——, and Coauthors, 2015: Validation of the summertime surface energy budget of Larsen C Ice Shelf (Antarctica) as represented in three high-resolution atmospheric models. *J. Geophys. Res. Atmos.,* 120, 1335–1347, doi:10.1002/2014JD022604.

Kuipers Munneke, P., M. R. van den Broeke, J. T. M. Lenaerts, M. G. Flanner, A. S. Gardner, and W. J. Van de Berg, 2011: A new albedo parameterization for use in climate models over the Antarctic ice sheet. *J. Geophys. Res.,* **116,** D05114, doi:10.1029/2010JD015113.

——, ——, J. C. King, T. Gray, and C. H. Reijmer, 2012: Near-surface climate and surface energy budget of Larsen C ice shelf, Antarctic Peninsula. *Cryosphere,* **6,** 353–363, doi:10.5194/tc-6-353-2012.

Lang, C., X. Fettweis, and M. Erpicum, 2015: Stable climate and surface mass balance in Svalbard over 1979–2013 despite the Arctic warming. *Cryosphere,* **9,** 83–101, doi:10.5194/tc-9-83-2015.

Lenaerts, J. T. M., M. R. van den Broeke, S. J. Déry, E. van Meijgaard, W. J. van de Berg, S. P. Palm, and J. Sanz Rodrigo, 2012a: Modeling drifting snow in Antarctica with a regional climate model: 1. Methods and model evaluation. *J. Geophys. Res.,* **117,** D05108, doi:10.1029/2011JD016145.

——, ——, C. Scarchilli, and C. Agosta, 2012b: Impact of model resolution on simulated wind, drifting snow and surface mass balance in Terre Adélie, East Antarctica. *J. Glaciol.,* **58,** 821–829, doi:10.3189/2012JoG12J020.

——, ——, W. J. van de Berg, E. van Meijgaard, and P. Kuipers Munneke, 2012c: A new, high-resolution surface mass balance map of Antarctica (1979–2010) based on regional atmospheric climate modeling. *Geophys. Res. Lett.,* **39,** L04501, doi:10.1029/2011GL050713.

——, ——, J. M. van Wessem, W. J. van de Berg, E. van Meijgaard, L. H. van Ulft, and M. Schaefer, 2014: Extreme precipitation and climate gradients in Patagonia revealed by high-resolution regional atmospheric climate modeling. *J. Climate,* **27,** 4607–4621, doi:10.1175/JCLI-D-13-00579.1.

Ligtenberg, S. R. M., M. M. Helsen, and M. R. van den Broeke, 2011: An improved semi-empirical model for the densification of Antarctic firn. *Cryosphere,* **5,** 809–819, doi:10.5194/tc-5-809-2011.

Liu, H., K. Jezek, B. Li, and Z. Zhao, 2001: Radarsat Antarctic Mapping Project Digital Elevation Model version 2. National Snow and Ice Data Center. [Available online at http://nsidc.org/data/docs/daac/nsidc0082_ramp_dem_v2.gd.html.]

Marshall, G., A. Orr, N. van Lipzig, and J. King, 2006: The impact of a changing Southern Hemisphere Annular Mode on Antarctic Peninsula summer temperatures. *J. Climate,* **19,** 5388–5404, doi:10.1175/JCLI3844.1.

Morris, E. M., and D. G. Vaughan, 2003: Spatial and temporal variation of surface temperature on the Antarctic Peninsula and the limit of viability of ice shelves. *Antarct. Res. Ser.,* **79,** 61–68, doi:10.1029/079ARS05.

Orr, A., G. J. Marshall, J. C. R. Hunt, J. Sommeria, C.-G. Wang, N. P. M. van Lipzig, D. Cresswell, and J. C. King, 2008: Characteristics of summer airflow over the Antarctic Peninsula in response to recent strengthening of westerly circumpolar winds. *J. Atmos. Sci.,* **65,** 1396–1413, doi:10.1175/2007JAS2498.1.

Parish, T. R., 1983: The influence of the Antarctic Peninsula on the wind field over the western Weddell Sea. *J. Geophys. Res.,* **88,** 2684–2692, doi:10.1029/JC088iC04p02684.

Powers, J. G., K. W. Manning, D. H. Bromwich, J. J. Cassano, and A. M. Cayette, 2012: A decade of Antarctic science support through AMPS. *Bull. Amer. Meteor. Soc.,* **93,** 1699–1712, doi:10.1175/BAMS-D-11-00186.1.

Reijmer, C. H., E. van Meijgaard, and M. R. van den Broeke, 2005: Evaluation of temperature and wind over Antarctica in a Regional Atmospheric Climate Model using 1 year of automatic weather station data and upper air observations. *J. Geophys. Res.,* **110,** D04103, doi:10.1029/2004JD005234.

Rignot, E., G. Casassa, P. Gogineni, W. Krabill, A. Rivera, and R. Thomas, 2004: Accelerated ice discharge from the Antarctic Peninsula following the collapse of Larsen B ice shelf. *Geophys. Res. Lett.,* **31,** L18401, doi:10.1029/2004GL020697.

Rott, H., F. Müller, T. Nagler, and D. Floricioiu, 2011: The imbalance of glaciers after disintegration of Larsen-B ice shelf, Antarctic Peninsula. *Cryosphere,* **5,** 125–134, doi:10.5194/tc-5-125-2011.

Scambos, T. A., 2004: Glacier acceleration and thinning after ice shelf collapse in the Larsen B embayment, Antarctica. *Geophys. Res. Lett.,* **31,** L18402, doi:10.1029/2004GL020670.

——, C. Hulbe, M. Fahnestock, and J. Bohlander, 2000: The link between climate warming and break-up of ice shelves in the Antarctic Peninsula. *J. Glaciol.,* **46,** 516–530, doi:10.3189/172756500781833043.

——, H. A. Fricker, C.-C. Liu, J. Bohlander, J. Fastook, A. Sargent, R. Massom, and A.-M. Wu, 2009: Ice shelf disintegration by plate bending and hydro-fracture: Satellite observations and model results of the 2008 Wilkins ice shelf break-ups. *Earth Planet. Sci. Lett.,* **280,** 51–60, doi:10.1016/j.epsl.2008.12.027.

Schwerdtfeger, W., 1975: The effect of the Antarctic Peninsula on the temperature regime of the Weddell Sea. *Mon. Wea. Rev.,* **103,** 45–51, doi:10.1175/1520-0493(1975)103<0045:TEOTAP>2.0.CO;2.

Tedesco, M., W. Abdalati, and H. J. Zwally, 2007: Persistent surface snowmelt over Antarctica (1987–2006) from 19.35 GHz brightness temperatures. *Geophys. Res. Lett.,* **34,** L18504, doi:10.1029/2007GL031199.

Turner, J., S. R. Colwell, G. J. Marshall, T. A. Lachlan-Cope, A. M. Carleton, P. D. Jones, and P. A. Reid, 2004: The SCAR READER Project: Toward a high-quality database of mean Antarctic meteorological observations. *J. Climate,* **17,** 2890–2898, doi:10.1175/1520-0442(2004)017<2890:TSRPTA>2.0.CO;2.

——, and Coauthors, 2005: Antarctic climate change during the last 50 years. *Int. J. Climatol.,* **25,** 279–294, doi:10.1002/joc.1130.

UCAR/NCAR/CISL/VETS, 2014: The NCAR Command Language Version 6.2.1. NCAR Computer Information Systems Laboratory, doi:10.5065/D6WD3XH5.

Undén, P., and Coauthors, 2002: HIRLAM-5 Scientific Documentation. Swedish Meteorology and Hydrology Institute Tech. Rep., 143 pp. [Available online at http://www.hirlam.org/index.php/meeting-reports-and-presentations/doc_view/308-unden-et-al-2002.]

Van Angelen, J. H., M. R. van den Broeke, and W. J. van de Berg, 2011: Momentum budget of the atmospheric boundary layer over the Greenland ice sheet and its surrounding seas. *J. Geophys. Res.,* **116,** D10101, doi:10.1029/2010JD015485.

Van den Broeke, M. R., J.-G. Winther, E. Isaksson, J. F. Pinglot, L. Karlöf, T. Eiken, and L. Conrads, 1999: Climate variables along a traverse line in Dronning Maud Land, East Antarctica. *J. Glaciol.,* **45,** 295–302, doi:10.3189/002214399793377266.

——, C. H. Reijmer, D. van As, R. van de Wal, and J. Oerlemans, 2005: Seasonal cycles of Antarctic surface energy balance from automatic weather stations. *Ann. Glaciol.,* **41,** 131–139, doi:10.3189/172756405781813168.

Van Lipzig, N. P. M., J. C. King, T. A. Lachlan-Cope, and M. R. van den Broeke, 2004: Precipitation, sublimation, and snow drift in the Antarctic Peninsula region from a regional atmospheric model. *J. Geophys. Res.,* **109,** D24106, doi:10.1029/2004JD004701.

——, G. J. Marshall, A. Orr, and J. C. King, 2008: The relationship between the Southern Hemisphere Annular Mode and

Antarctic Peninsula summer temperatures: Analysis of a high-resolution model climatology. *J. Climate,* **21,** 1649–1668, doi:10.1175/2007JCLI1695.1.

Van Wessem, J. M., C. H. Reijmer, J. T. M. Lenaerts, W. J. van de Berg, M. R. van den Broeke, and E. van Meijgaard, 2014a: Updated cloud physics in a regional atmospheric climate model improves the modelled surface energy balance of Antarctica. *Cryosphere,* **8,** 125–135, doi:10.5194/tc-8-125-2014.

——, and Coauthors, 2014b: Improved representation of East Antarctic surface mass balance in a regional atmospheric climate model. *J. Glaciol.,* **60,** 761–770, doi:10.3189/2014JoG14J051.

Wendler, G., N. Ishikawa, and Y. Kodama, 1988: The heat balance of the icy slope of Adelie Land, Eastern Antarctica. *J. Appl. Meteor.,* **27,** 52–65, doi:10.1175/1520-0450(1988)027<0052:THBOTI>2.0.CO;2.